Mitigation strategies against radiation-induced background for space astronomy missions

Journal Item

Prepared for submission to JINST

Mitigation strategies against radiation-induced background for space astronomy missions

C. S. W. Davis, D. Hall, J. Keelan, J. O'Farrell, M. Leese, and A. Holland

Centre for Electronic Imaging, The Open University,
Milton Keynes, MK7 6AA, United Kingdom

E-mail: Chris.Davis@open.ac.uk

Abstract: The Advanced Telescope for High ENergy Astrophysics (ATHENA) mission is a major upcoming space-based X-ray observatory due to be launched in 2028 by ESA, with the purpose of mapping the early universe and observing black holes. Background radiation is expected to constitute a large fraction of the total system noise in the Wide Field Imager (WFI) instrument on ATHENA, and designing an effective system to reduce the background radiation impacting the WFI will be crucial for maximising its sensitivity. Significant background sources are expected to include high energy protons, X-ray fluorescence lines, 'knock-on' electrons and Compton electrons. Due to the variety of the different background sources, multiple shielding methods may be required to achieve maximum sensitivity in the WFI. These techniques may also be of great interest for use in future space-based X-ray experiments. Simulations have been developed to model the effect of a graded-Z shield on the X-ray fluorescence background. In addition the effect of a 90nm optical blocking filter on the secondary electron background has been investigated and shown to modify the requirements of any secondary electron shielding that is to be used.

Keywords: X-ray, radiation, magnetic diverter, knock-on electrons, ATHENA, instrument background

Contents

1 Introduction

Cosmic background radiation is a large background component within any space astronomy mission. The nature of such background radiation varies with orbit location, detector type and the solar cycle. In the case of the Wide Field Imager (WFI) [1, 2] on the Advanced Telescope for High ENergy Astrophysics (ATHENA) mission [3, 4], for higher energies this background noise is expected to primarily originate from secondary sources within the materials surrounding the detector [5, 6].

Some characteristics of the WFI are given in Table 1. The WFI will consist of two DEPleted Field Effect Transistor (DEPFET) array detectors; a large area detector comprised of four sensors and a total of 1064×1064 pixels for imaging across a wide spectral band, and a high count rate 64×64 pixel detector for high resolution images of brighter objects. The high count rate detector will be capable of observing objects of approximately 1 Crab in intensity with a pile-up of less than 1% and a throughput of more than 80%. The DEPFETs within these detectors will contain depletion layers of $\approx 450 \mu m$, and will be backside illuminated.

Photons will be directed to either the WFI or X-ray Integral Field Unit (XIFU) [7] instrument by a mirror system, then will pass through a baffle and through a filter wheel to the WFI. The filter wheel contains filters suited for multiple purposes such as the attenuation of straylight and

Table 1: Some characteristics of the ATHENA Wide Field Imager (WFI) [9].

WFI Characteristics	
Large Area Detector Field Of View	40 arcmin × 40 arcmin
Energy Detection Range	0.1 - 15 keV
Spectral Resolution	<150 eV at 6 keV
Time Resolution	~8 μs full window mode, ~1.3 ms full frame
Count-Rate Capacity	~1 Crab
Non-X-ray Background (L2 orbit)	$< 5 \times 10^{-3}$ ct cm^{-2} s^{-1} keV^{-1}
Quantum Efficiency	>20% for 277 eV >80% for 1 keV >90% for 10 keV

calibration. Each filter is independently designed for use with either the high count rate detector or large area detector.

A background count rate of 5×10^{-3} cts / cm^2 / s / keV has been set as the baseline target requirement for both the ATHENA WFI and XIFU. The most important secondary background noise sources are predicted to be secondary electrons and X-ray fluorescence lines [8], both of which are expected to exceed the target background count rate at certain parts of the spectrum. Determining methods to reduce these components will be important if the science capabilities of both ATHENA and future X-ray astronomy missions are to be met and maximised.

2 Instrument background sources

Due to the high sensitivity requirements of the WFI, significant background noise sources are not only expected to consist of particles which enter the aperture of ATHENA, but from secondary sources generated within the spacecraft. Characterising the effect of each secondary background source on the observed signal will be necessary for both simulating the signal to noise ratio in the WFI, as well as designing mitigation strategies to reduce these effects.

2.1 Compton scattering

As the WFI is a relatively thick detector, Compton scattering of photons through the device may create a prominent source of noise in the WFI, more so than that found in the CCDs in XMM-Newton for example [10]. This effect of this Compton background on the WFI has not been investigated in detail at present, although it will need to be characterised for a full prediction of the WFI's background noise to be created, and potentially so that further shielding methods may be developed, such as through the addition of a thin high-Z outer shield.

2.2 Secondary electrons

Secondary electrons are expected to form one of the largest components of background across nearly the full energy range of 0.1keV - 15keV.

Secondary electrons are produced when a high energy proton passes through a material. A useful metric for characterising the distance a particle will travel in a material is the Continuous

Slowing Down Approximation range (CSDA range). The CSDA range is an approximation of a particle's average path length in a material, calculated through the assumption that the rate of energy loss of the particle with respect to time is equal to the total stopping power of the material. Within the 0.1keV - 15keV range of electron energies, the CSDA range of secondary electrons through aluminium is on the order of microns, and so the majority of electrons hitting the detector originate from the top few microns on a particular surface.

These electrons are expected to be nearly indistinguishable in the WFI from a photon with the same energy. This is because the mean free path of electrons through silicon is small relative to the WFI thickness, so all of an electron's energy will be deposited within a single pixel. The signal produced by such an electron is unlikely to be able to be removed computationally, because unlike high energy protons for example they will not leave visible, distinguishable tracks through multiple pixels in images produced by the WFI.

Electrons with energies greater than 15keV would normally be outside the energy window of the WFI, however the WFI will have a 90nm optical blocking filter placed on-chip. As discussed in Section 5.2, the optical blocking filter will likely remove energy from secondary electrons impacting it, and therefore also cause further secondary electrons to be created at all energies.

2.3 Secondary X-rays

Secondary X-rays are typically created through bremsstrahlung, fluorescence and PIXE (Particle Induced X-ray Emission) within materials surrounding space-based detectors. Attenuation lengths vary extensively depending on the attenuating material and photon energy. In aluminium this is on the order of μm, meaning that almost all secondary X-rays that will influence the background noise in the WFI will originate from surfaces within line-of-sight of the WFI. Energies produced by PIXE depend on the inner shell electron ionisation energies of elements within the material, which drop as atomic number decreases. This leads to the concept of a graded-Z shield, as described in section 3.2.

Three Al K_α and K_β fluorescence lines are expected to appear as a result of PIXE on the WFI spectrum, at 1.487, 1.486 and 1.557 keV. These fluorescence lines are expected to create a count rate significantly larger than the target count rate, even without the extra contribution from the secondary electron spectrum.

3 Mitigation techniques

As discussed in the previous section, multiple secondary instrument background sources are expected to significantly add to the signal that the ATHENA WFI will observe. As there are expected to be multiple sources of secondary background noise in the WFI, multiple mitigation strategies will likely need to be employed which are specific to each secondary background noise source.

3.1 Magnetic diversion

Magnetic shielding falls into two categories - active shielding and passive shielding. Active shielding refers to, for example, magnetic shielding that can be varied in strength or direction, such as that consisting of electromagnets, whereas passive shielding would consist of permanent magnets attached to the spacecraft. Magnetic diversion has been used for several decades within the context

of shielding space-based detectors from charged particles [11]. The current proposed ATHENA design already contains a magnetic diverter at its aperture [12], designed to divert incoming electrons into the baffle of the telescope before they can reach any instruments that are sensitive to them. To shield secondary electrons in ATHENA, however, would require magnetic fields surrounding the WFI shielding as opposed to the baffle.

In general, the use of permanent magnets is preferable to electromagnets, because the engineering requirements of such a system would include a power supply and associated electronics, which would be more prone to failure, and increase the complexity of the overall spacecraft design.

Protons of > 60keV are likely too massive and too energetic to be reasonably deflected using magnets. However secondary electrons of energies between 0.1keV - 15keV are well within the energy range that can be deflected by a simple neodymium bar magnet, a possibility that will be investigated in the future.

3.2 Graded-Z shielding

Graded-Z shielding [13] is designed to remove secondary X-ray fluorescence lines from the background. The design relies on Moseley's Law [14], that the energy of K_α and K_β fluorescence lines decrease as atomic number decreases, in accordance with $E \propto Z^2$, and the fact that K_α and K_β fluorescence yield decreases with atomic number [15]. The aim is to coat a material with another material with a lower atomic number which will emit X-rays at a lower energy and at a lower fluorescence yield, while absorbing the X-rays from the substrate material. Further materials with sequentially lower Z can be layered on to this structure, moving toward the inner surface of the shielding, to reduce the energy of fluorescence until it will no longer fall within the detector's energy range. Coating the materials surrounding the WFI rather than the attaching of plates to them would be preferable because a coating would take up less space, although a thin plating may also be suitable.

The difficulty in the case of the WFI is finding materials consisting of elements with lower atomic numbers than aluminium that is suitable for use in a space-based environment. Several materials for potential investigation are boron, carbon, beryllium or combinations of these. One potential material that may be able to be used is boron carbide (B_4C). Boron carbide has excellent mechanical properties of strength and hardness, however it has a coefficient of thermal expansion that is significantly smaller than that for Al, meaning that if it were attached to an aluminium surface, there is a possibility that boron carbide might crack under the large temperature variations that can occur in space missions.

One possible solution to this potential problem is investigated in Section 4.1: to embed grains of B_4C inside aluminium; this is known as a 'mixed metal matrix' [16]. While an Al-B_4C metal matrix composite is unlikely to absorb fluorescence X-rays as effectively as a pure boron carbide shield, it may be able to strike a compromise between the engineering necessities and sensitivity requirements of the WFI. Alternatively it could act as a material upon which pure boron carbide might be able to be more easily deposited.

A model can be created to approximate the output fluorescence of such a material at the aluminium K_α and K_β wavelengths. The intensity of a fluorescence line at a specific energy at different positions through a material which is being bombarded with high energy protons from all sides can be modeled with Equation (3.1), where z is the distance through the material, μ is

the linear X-ray attenuation coefficient for the material, and G is a factor representing the number of extra fluorescence lines that are created within a small layer of the material by protons passing through the material.

$$\frac{dI(z)}{dz} = -\mu(z)I(z) + G(z) \tag{3.1}$$

The general solution to Equation (3.1) is Equation (3.2), where I_0 is the initial intensity entering the material.

$$I(z) = I_0 e^{-\int_0^z \mu(\epsilon)d\epsilon} + \int_0^z G(\gamma)e^{-\int_\gamma^z \mu(\epsilon)d\epsilon} d\gamma \tag{3.2}$$

In Equation (3.2), γ and ϵ simply represent integration constants. Equation (3.2) can be physically interpreted as a sum of the initial intensity remaining at z after attenuation (the first term in Equation (3.2)), plus the sum of fluorescence generated at all points between 0 and z, after attenuation to z (the second term in Equation (3.2)). Assuming that the material can be approximated as being uniform and homogeneous, and that proton flux is constant throughout the material, Equation (3.2) reduces to Equation (3.3).

$$I(z) = I_0 e^{-\mu z} + \frac{G}{\mu}(1 - e^{-\mu z}) \tag{3.3}$$

Finally, if the material thickness is significantly greater than the attenuation length λ in the material, which is equal to $\frac{1}{\mu}$, Equation (3.3) reduces to Equation (3.4).

$$I(z) \approx \frac{G}{\mu} = G\lambda \tag{3.4}$$

In aluminium, the attenuation length for X-rays is on the order of microns to tens of microns, depending on x-ray energy. Equations (3.3) and (3.4) illustrate the two competing factors that must be modified in a graded-Z shield. G must be reduced, while μ is made larger.

Any element with sufficiently low Z should not fluoresce in the range that the WFI will detect, and thus G should be effectively zero for such materials at aluminium fluorescence line energies, however in the case of an Al-B_4C metal matrix composite, if the material is approximated to be uniform, it will have a non-zero effective G. It should be noted however that G will be non-zero at energies at the boron (0.183keV) and carbon (0.277keV) fluorescence lines [17], although these fluorescence lines have a lower fluorescence yield than the aluminium K_α and K_β lines, and more materials can be layered onto the mixed metal matrix layer to attenuate these fluorescence lines further, such as diamond-like carbon for instance.

At the aluminium fluorescence lines, if the effective G is simply the mean value of G across an infinitesimal layer in the material, then $G_{eff} = G(1 - r)$, where r is the volume percentage of B_4C in the material. Assuming that the attenuation coefficient of Al-B_4C is simply the mean attenuation coefficient of the material, then this means that inserting G_{eff} into eq. (3.4) gives Equation (3.5).

$$\frac{I_{Al-B_4C}}{I_{Al}} = \frac{(1 - r)\mu_{Al}}{r\mu_{B_4C} + (1 - r)\mu_{Al}} \tag{3.5}$$

The analysis relating to this equation is presented in Section 5.1. In Section 4.1, a simulation method for determining the attenuation coefficient of Al-B_4C is discussed.

4 Simulation methods

Geant4 [18] is a Monte Carlo simulations program that was initially developed by CERN to perform high energy particle simulations, but has been used for a variety of space-based applications in recent years. Geant4 uses numerical methods in calculating particle trajectories and interactions, and this can lead to errors depending on which numerical methods and approximations are used. This means that comparison of Geant4 simulations to experimental data is vital in verifying Geant4 results.

4.1 Aluminium boron carbide mixed metal matrix simulations

A mixed metal matrix in this case was modeled by converting a specified cuboid shape of the material into a discrete lattice, and then randomly distributing boron carbide sphere centers one by one on the lattice in such a way that no sphere centers overlap. This was performed by converting the cuboid into a discrete lattice, and placing spheres sequentially until either no permitted lattice points existed any more, or when the number of ratio of sphere volume to cuboid volume exceeds the specified B_4C / Al ratio. The form of the geometries generated by this process is shown in Figure 1a, while Figure 1b gives the mean density at each point over 100 different randomly generated geometries. Due to the statistical nature of random generation, mixed metal matrix generation would often fail for B_4C / Al ratios above a certain value depending on the system geometry. In Section 5.1, ratios greater than 0.2 have been unable to be yet achieved, although it appears it may be possible in future simulations to generate higher ratios by varying geometry and sphere size.

Each run of the simulation involved placing a photon at $(x, y) = (0, 0)$ where the cuboid center was at $(x, y, z) = (0, 0, 0)$, and momentum was oriented in the z-direction. If the photon, or any by-products of the photon's interactions successfully exited the material without being absorbed, a 'hit detector' would record the particle's mass, position and energy. As the purpose of this simulation was to find the attenuation coefficients of the material, only output particles with identical properties to the initial input particle were counted. Assuming that the material can be treated as uniform, the probability of a particle successfully reaching the hit detector without being absorbed by the material should be $e^{-\mu t}$ where t is equal to the thickness of material the particle travels through. Therefore the attenuation coefficient can be found by sending photons through varying thicknesses of the material and recording the ratio that successfully reach the hit detector. Thicknesses were varied by varying the distance of the particle generation location to the detector, while initial momentum was always oriented in the z-direction.

Because Al-B_4C in this case has a random structure, it would be ideal if for every run the structure could be re-generated to find the mean attenuation coefficient. However, the geometry generation process took too long for this to be feasible. Instead, the structure was re-generated for each change in thickness, while a varying structure was approximated within runs of the same thickness by randomising the x and y position of each particle.

4.2 The effect of an optical blocking filter on the secondary electron count

As discussed in Section 2.2, the optical blocking filter to be placed on-chip will likely create more secondary electrons when bombarded with high energy secondary electrons. For this reason, simulations were performed to study the secondary electron spectrum produced when an electron of a given energy impacts the optical blocking filter. The simulation used in Section 4.1 was modified

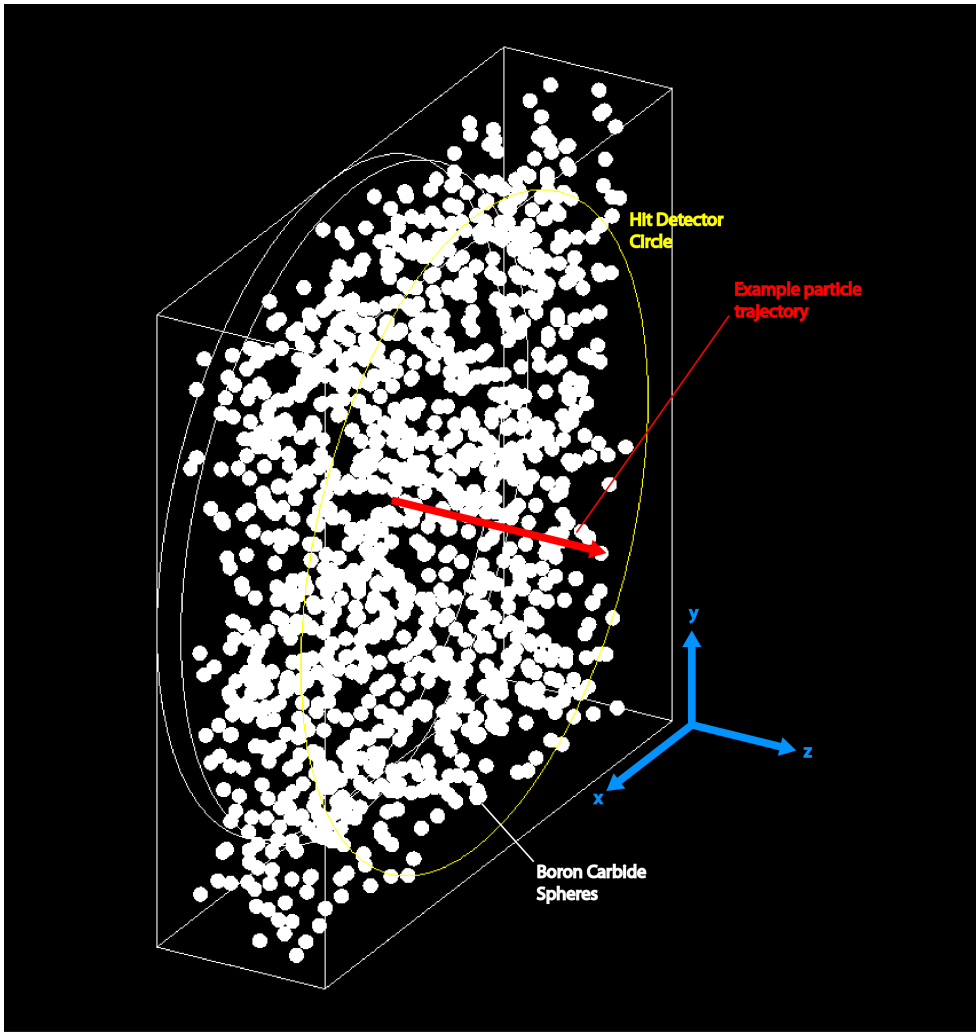

(a) An image of an example boron carbide mixed metal matrix geometry randomly generated for Geant4 simulations. White spheres here represent boron carbide, which are embedded within an aluminium cuboid. When a particle hits the 'hit detector' circle, the energy, mass and position of the particle are recorded.

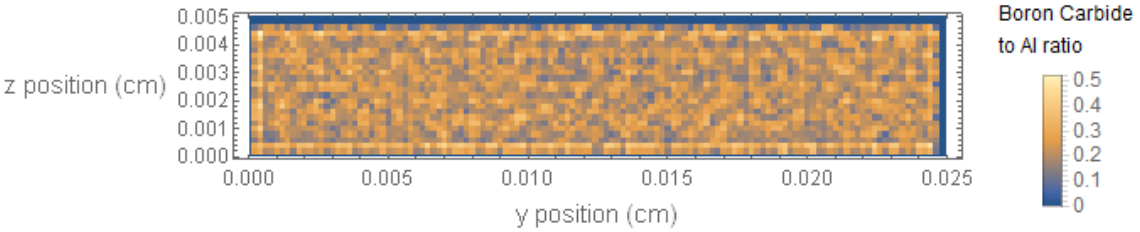

(b) A histogram displaying the density of spheres averaged over 100 randomly generated geometries of the form displayed in Figure 1a. This plot displays the large statistical variance present in the density and mean density over 100 geometries. In this case the x-position was 0 for all runs, where the cuboid of aluminium was centered at (0,0,0). On this diagram a bright rectangle of high density can be seen surrounding the solid, however the density aside from this seems to be approximately random, as intended.

Figure 1: The geometry set up used to describe Al-B_4C metal matrix composites in the simulations described in Section 4.1. Figure 1a shows an example of a 3D geometry that random sphere placing produces, and Figure 1b displays the densities for such geometries, averaged over 100 generations.

to calculate transmittance ratios for electrons traveling through a 90nm aluminium plate. Input photons were replaced with electrons, and boron carbide spheres were removed from the geometry generation. The number of output electrons at energies between between 0.1keV and 15keV were collected and counted for incoming electrons of energies between 0.1keV and 15keV. Electrons at higher energies also needed to be simulated, because the optical blocking filter will lower the energy of many incoming electrons, and generate extra electron flux at lower energies. Outgoing X-rays were included in the outputted count, because electrons passing through the optical blocking filter would fluorescence as a result of PIXE and bremsstrahlung. Results for this simulation are displayed and discussed in Section 5.2.

5 Simulated results

5.1 Aluminium boron carbide mixed metal matrix simulations

The attenuation coefficient of Al-B_4C with 20% B_4C can be seen in Figure 2. Here, spheres with a radius of 3μm were used to model grains of B_4C. It appears that for energies near the aluminium fluorescence lines, that the Geant4 simulations perform reasonably, however there seems to be some divergence of Geant4 predicted attenuation coefficients from tabulated and predicted results at higher energies. Because this divergence represents an increase rather than decrease in attenuation coefficient, it is unlikely that this is because of a missing physical process from Geant4 simulations.

It is also unlikely that this discrepancy is caused by coherent (for instance Rayleigh scattering) or incoherent scattering (Compton scattering) processes being modeled in Geant4 but not in tabulated data, as the attenuation coefficients for X-Rays of energies between 1keV and 15keV for such processes are [19] $0.85cm^{-1} < \mu < 6.09cm^{-1}$ for coherent scattering and $0.039cm^{-1} < \mu < 0.34cm^{-1}$ for incoherent scattering, and are therefore small relative to the total attenuation coefficients displayed in fig. 2.

To confirm that the cross-sections for Rayleigh scattering and Compton scattering that Geant4 used were in fact negligible, simulations were run using a modified version of the above software with spheres removed altogether; in previous aluminium simulations spheres were set to be made of aluminium rather than B_4C as opposed to being removed entirely. These new simulations calculated the attenuation coefficients of a $5keV$ X-Ray traveling through aluminium, with all scattering processes turned on, and with Compton and Rayleigh scattering turned off. The simulation with scattering turned on returned an attenuation coefficient of $532cm^{-1} \pm 0.5cm^{-1}$, and the simulation with Compton and Rayleigh scattering turned off returned an attenuation coefficient of $522cm^{-1} \pm 0.5cm^{-1}$(0 decimal places). As these values seem to adhere to tabulated aluminium attenuation coefficients reasonably well, it seems that the discrepancy may be due to the sphere distribution in previous simulations in Geant4.

The adherence to the model given in Section 3.2 near the fluorescence lines however would give some indication that the sphere model is a reasonable first approximation near this energy. From the model results it appears unlikely that an Al-B_4C graded-Z shield should be effective at removing a fluorescence line completely from the signal. Equation (3.5) implies that for a value of $r = 0.5$, output intensities for Al-B_4C below the fluorescence line energies will be approximately halved, because the attenuation coefficients at this energy and densities of boron carbide and aluminium are

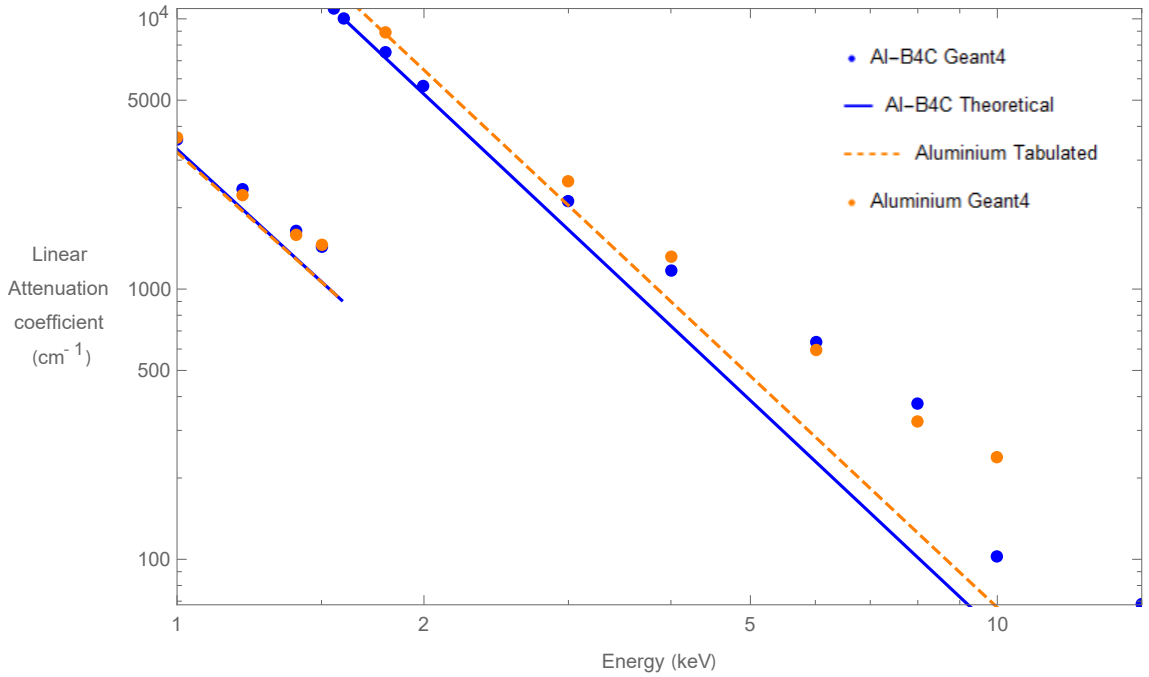

Figure 2: The attenuation coefficient of Al-B_4C as a function of X-Ray energy. Here the orange dotted line represents the attenuation coefficient of aluminium [20], and the solid blue line represents the predicted Al-B_4C attenuation coefficient using Equation (3.1). Points represent simulation data points for aluminium (orange), and Al-B_4C (blue).

almost identical at these energies. However, at energies greater than the fluorescence energies, the attenuation coefficient of aluminium is much larger than the attenuation coefficient of boron carbide, meaning that the decrease in generation of X-Rays with increasing r is approximately canceled out by decrease in attenuation coefficient with increasing r.

Due to emission line spreading because of for instance, thermal effects, some X-Rays would be produced at energies slightly lower than the fluorescence energies, and some at greater energies, but only intensities of lower energies would be effectively reduced by an Al-B_4C shield of $r = 0.5$, and only by half. Should this model and analysis be correct, this means that an Al-B_4C graded-Z shield may not be suitable for the WFI unless it is layered with other materials, although this analysis will need to be tested further.

5.2 Optical blocking filter simulations

The simulations of Al-B_4C did not include the effect of the ATHENA geometry on the requirements for the graded-Z shielding, and in particular did not include the effect of the on-chip optical blocking filter.

As discussed in Section 4.2, the optical blocking filter placed upon the WFI DEPFETs will alter the observed spectrum, and characterising the filter's effect on the spectrum of both secondary electrons and secondary X-rays is necessary to calculate the full effectiveness of all forms of secondary background shielding.

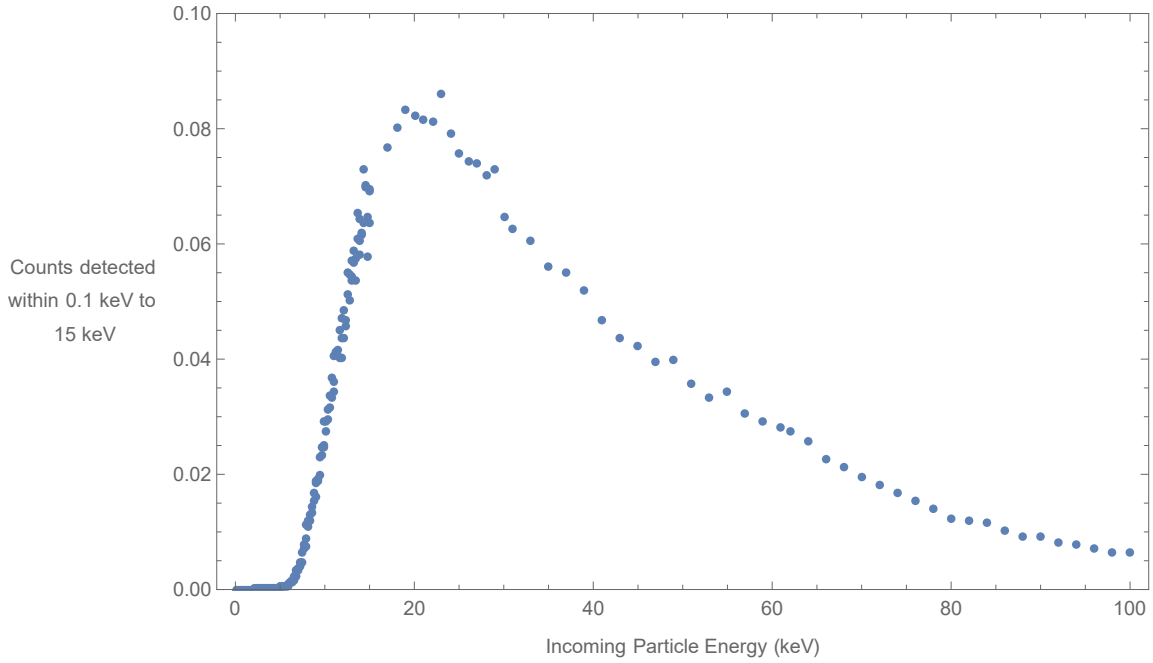

Figure 3: The total number of electrons received between the range of 0.1keV - 15keV through a 90nm aluminium layer, for given energies of input electrons.

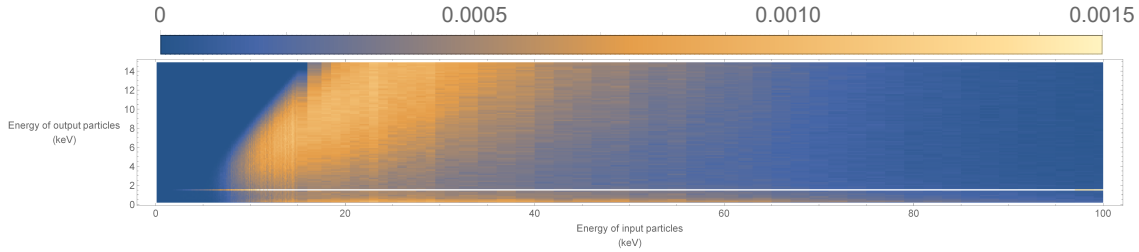

Figure 4: The count rate received through a 90nm aluminium optical blocking filter when an electron of a given input energy between 0.1keV and 100keV impacts the optical blocking filter perpendicular to its surface. Incoming electron energies are represented at the middle of each cuboid, and output energies were binned at bin widths of 0.149keV, and the ratio of incoming electron number to outgoing particle number was averaged over 1×10^6 particles. The sharp horizontal line near output energies of 1.5keV can be identified as the fluorescence lines of aluminium.

Optical blocking filter simulation data are shown in Figure 3. The figure shows that many incoming electrons will generate secondary electrons as they pass through the filter, at lower energies. This means that the presence of secondary electrons at energies greater than the detection range cannot be ignored as has been previously assumed. Depending on the form of the secondary electron spectrum at higher energies this may increase or decrease the detector noise.

The full effect of an optical blocking filter on the secondary electron spectrum can be seen in Figure 4, as described in Section 4.2.

The aluminium K_α fluorescence lines near 1.5keV can be observed as a peak for all input

energies in Figure 4. To fully analyse these results it will be necessary to use the full predicted secondary electron flux impacting the optical blocking filter to obtain the recorded output signal, however Figure 4 does appear to show that if the input flux were constant across the spectrum, then the secondary electron flux would also be approximately constant.

Another factor to consider is that these simulations were performed with all electrons impacting the optical blocking filter perpendicularly to its surface, whereas in the real WFI, secondary electrons will originate from a range of angles. This may act to simply increase the effective thickness of the optical blocking filter due to the greater distance electrons will have to travel through the aluminium, or it could lead to a more complicated effect on the spectrum, because the angle secondary particles will be produced at relative to the initial electron's trajectory may vary with their energy.

6 Conclusions

Methods for shielding the WFI from aluminium fluorescence and secondary electron background have been considered. The model constructed in Section 3.2 implies that an aluminium-boron-carbide metal matrix composite graded-Z shield may not be effective in removing aluminium fluorescence completely, but this model has yet to be properly tested through simulation.

Additionally, magnetic diversion has been considered as a method to shield the ATHENA WFI from secondary electrons. It is expected that the on-chip aluminium optical blocking filter to be placed on top of the WFI DEPFETs may significantly alter the secondary electron background present within the detector, and any potential requirements for any magnetic diversion shielding surrounding the detector. It is likely that methods of reducing the count rate of secondary electrons at higher than the 15keV maximum detection energy of the detector will have to be considered, as these will generate electrons within the energy range of the WFI upon impacting the optical blocking filter. This means that any secondary electron magnetic diversion techniques that could potentially be used on ATHENA may have to be capable of diverting electrons with greater energies than the energy detection range of the WFI.

Future work will need to verify the Geant4 simulations performed here through comparison with experimental results, and simulations of metal matrix composites with B_4C to Al ratios of greater than 0.2 will be also need to be performed.

References

[1] N Meidinger et al. The wide field imager instrument for athena. *Proc. SPIE*, 9905:9905 – 9905 – 12, 2016. doi: 10.1117/12.2231604.

[2] A Rau et al. The hot and energetic universe: The wide field imager (wfi) for athena+. *arXiv preprint arXiv:1308.6785*, 2013.

[3] K Nandra et al. The Advanced Telescope for High-Energy Astrophysics. *ESA*, pages 1–36, 2012.

[4] X Barcons, K Nandra, D Barret, J-W den Herder, A C Fabian, L Piro, M G Watson, and the Athena team. Athena: the X-ray observatory to study the hot and energetic Universe. *J. Phys.: Conf. Ser*, 610, 2015.

[5] E Perinati, S Diebold, A Guzman, A Santangelo, and C Tenzer. Background studies for ATHENA: status of the activities at IAAT. doi: 10.1117/12.2231599.

[6] S Hauf. *Studies on the Background of the Wide Field Imager aboard the IXO and ATHENA X-Ray Telescopes*. PhD thesis, Technische Universitat Darmstadt, 2012.

[7] E Perinati, A Santangelo, and C Tenzer. Background studies for athena: towards a new assessment phase. In *Proc. of SPIE*, volume 9144, pages 91445Y–1, 2014.

[8] S Hauf et al. Background simulations of the wide field imager of the ATHENA X-ray observatory. pages 1239–1243, 2012. ISSN 10957863. doi: 10.1109/NSSMIC.2011.6154609.

[9] N Meidinger et al. Development of the wide field imager for athena. In *SPIE Optical Engineering+ Applications*, pages 96010H–96010H. International Society for Optics and Photonics, 2015.

[10] D. Hall and A. Holland. Space radiation environment effects on x-ray ccd background. *Nuclear Instruments and Methods in Physics Research Section A: Accelerators, Spectrometers, Detectors and Associated Equipment*, 612(2):320–327, 2010.

[11] M Turner. A Magnetic Diverter for Charged Particles on XEUS. *ESA document SCI-SA/AP/06/0412cv*, 2006.

[12] S Lotti et al. Updates on the background estimates for the x-ifu instrument onboard of the athena mission. In *SPIE Astronomical Telescopes+ Instrumentation*, pages 99055S–99055S. International Society for Optics and Photonics, 2016.

[13] W.C. Fan, C.R. Drumm, S.B. Roeske, and G.J. Scrivner. Shielding considerations for satellite microelectronics. *IEEE Transactions on Nuclear Science*, 43(6):2790–2796, 1996. ISSN 00189499. doi: 10.1109/23.556868.

[14] H. Moseley. Xciii. the high-frequency spectra of the elements. *The London, Edinburgh, and Dublin Philosophical Magazine and Journal of Science*, 26(156):1024–1034, 1913.

[15] W. Bambynek et al. X-ray fluorescence yields, auger, and coster-kronig transition probabilities. *Rev. Mod. Phys.*, 44:716–813, Oct 1972. doi: 10.1103/RevModPhys.44.716.

[16] E. Mohammad Sharifi, F. Karimzadeh, and M.H. Enayati. Fabrication and evaluation of mechanical and tribological properties of boron carbide reinforced aluminum matrix nanocomposites. *Materials & Design*, 32(6):3263–3271, jun 2011. ISSN 02613069. doi: 10.1016/j.matdes.2011.02.033.

[17] G Kaye and T Laby. *Tables of Physical and Chemical Constants and Some Mathematical Functions*. HardPress Publishing, 2013.

[18] S. Agostinelli et al. Geant4 - a simulation toolkit. *Nuclear Instruments and Methods in Physics Research Section A: Accelerators, Spectrometers, Detectors and Associated Equipment*, 506(3): 250–303, 2003. ISSN 01689002. doi: 10.1016/S0168-9002(03)01368-8.

[19] J. Hubbell and S. Seltzer. Tables of X-Ray Mass Attenuation Coefficients and Mass Energy-Absorption Coefficients (version 1.4) [Online]. National Institute of Standards and Technology, Gaithersburg, MD, 2004. URL http://physics.nist.gov/xaamdi. Accessed 01/08/2017.

[20] B Henke, E Gullikson, Davis, B. L. Henke, E. M. Gullikson, and J. C. Davis. X-Ray Interactions: Photoabsorption, Scattering, Transmission, and Reflection at E = 50-30,000 eV, Z = 1-92. *Atomic Data and Nuclear Data Tables*, 54(2):181–342, jul 1993. ISSN 0092640X. doi: 10.1006/adnd.1993.1013.